The Generation of Superinertial Coastally Trapped Waves by Scattering at the Coast

R. C. MUSGRAVE,[a,b] D. WINTERS,[c] V. E. ZEMSKOVA,[c] AND J. A. LERCZAK[c]

[a] *Dalhousie University, Halifax, Nova Scotia, Canada*
[b] *Woods Hole Oceanographic Institution, Woods Hole, Massachusetts*
[c] *Oregon State University, Corvallis, Oregon*

(Manuscript received 14 September 2023, in final form 12 March 2024, accepted 25 March 2024)

ABSTRACT: A series of idealized numerical simulations is used to examine the generation of mode-one superinertial coastally trapped waves (CTWs). In the first set of simulations, CTWs are resonantly generated when freely propagating mode-one internal tides are incident on the coast such that the angle of incidence of the internal wave causes the projected wavenumber of the tide on the coast to satisfy a triad relationship with the wavenumbers of the bathymetry and the CTW. In the second set of simulations, CTWs are generated by the interaction of the barotropic tide with topography that has the same scales as the CTW. Under resonant conditions, superinertial coastally trapped waves are a leading order coastal process, with alongshore current magnitudes that can be larger than the barotropic or internal tides from which they are generated.

KEYWORDS: Continental shelf/slope; Inertia–gravity waves; Internal waves; Kelvin waves; Topographic effects; Wave properties

1. Introduction

Diapycnal mixing associated with breaking internal waves plays an important role in the physical dynamics of the ocean as, to leading order, it determines its interior stratification, with consequences for large-scale circulation and climate (de Lavergne et al. 2022). In the deep ocean, the astronomically forced tidal wave—well approximated by a Kelvin wave—interacts with rough topography to generate freely propagating internal tides, which radiate energy throughout the ocean basin predominantly in the form of vertical mode-one inertia–gravity waves[1] (Simmons et al. 2004). At the coast, cross-isobath currents associated with the topographically modified Kelvin wave (equivalently called the gravest coastal trapped wave) can generate significant internal tides that radiate into the ocean's interior (Baines 1982). The energy pathway toward dissipation for low-mode internal tides is not well quantified, though in the open ocean it is thought that both topographic scattering (St. Laurent and Garrett 2002) and nonlinear wave–wave interactions (MacKinnon and Winters 2005) are important. Significant low-mode energy is incident on coastal boundaries where the waves may reflect, scatter, or dissipate. In an analytic study that decomposed the global coasts into two-dimensional cross-shelf/depth slices with no alongshore variability, Kelly et al. (2013) predicted that globally around 40% of freely propagating mode-one internal tides incident on a uniform alongshore coast scatter to high vertical modes, with the precise scattering fraction depending on the slope steepness, height, and curvature. However, by allowing for alongshelf topographic variability, wave scattering at the coast can also generate alongshore propagating coastally trapped waves, a process that has been analyzed for unstratified fluids by Howe and Mysak (1973) and observed in stratified simulations of the Tasman Shelf, where they are predicted to locally account for a significant fraction of the local energy budget (Klymak et al. 2016).

In this paper, we consider the effect of alongshore topographic variability on both a topographically modified Kelvin wave propagating along the coast and an incident vertical mode-one inertia–gravity wave, with a focus on the scattering of wave energy into superinertial mode-one coastally trapped waves (CTWs). This scattering represents a pathway for superinertial tidal energy to move toward small scales in the coastal ocean. Superinertial CTW can exist along a continental shelf when $H_y N_{\mathrm{bot}}/f > 1$ (where H_y is the bottom slope of the continental slope in the offshore direction, N_{bot} is the bottom stratification frequency, and f is the Coriolis frequency) (Huthnance 1978; Chapman 1983). These waves are coupled to the freely propagating inertia–gravity waves of the ocean interior, "leaking" energy into offshore radiating waves while propagating along the coast (Dale and Sherwin 1996; Dale et al. 2001).

The scattering of barotropic shelf waves into either higher mode barotropic shelf waves or freely propagating inertia–gravity waves has been examined before. Scattering into other barotropic shelf waves by coastal irregularities has been considered within the context of wind-driven waves, though it is directly applicable to subinertial surface tides, for example, the diurnal tides at latitudes poleward of 30°N (Chao et al. 1979; Brink 1980). In particular, Brink (1980) found that the

[1] IGWs are commonly referred to as internal waves (or internal tides, if at tidal frequencies), but as many other types of waves (including CTWs) include internal or vertical structure, we will often use the former term in this paper to avoid ambiguity.

Denotes content that is immediately available upon publication as open access.

Corresponding author: R. C. Musgrave, rmusgrave@dal.ca

DOI: 10.1175/JPO-D-23-0180.1

rate of energy loss due to frictional damping of a barotropic CTW is comparable to scattering, where the scattering process is determined by a wave triad resonance between the topographic wavelength, and incident and scattered CTW. The stratified case has been examined by Brink (1986), and more recently by Kelly and Ogbuka (2022), who has made estimates of the generation of CTW by scattering from the subinertial surface tide at coastal promontories and along the Oregon shelf. As in the unstratified case, scattering into higher modes satisfies a resonance condition, occurring preferentially when the scales of the topography match those of the CTW. The scattering of barotropic shelf waves into freely propagating inertia–gravity waves at coastal irregularities has also been examined by Yankovsky and Zhang (2017), who found that changes in shelf width can generate large internal tides as the tidal Kelvin wave adjusts to alongshore changes.

In the open ocean, the scattering of inertia–gravity waves from small, subcritical bottom topography was considered by Müller and Xu (1992), who showed that scattering tends to transfer energy to smaller scales where it is more likely to steepen and break, contributing to ocean turbulence and mixing. Similar physics underlies the interaction of a corrugated vertical coastline with incident inertia–gravity waves in an unstratified fluid as considered by Howe and Mysak (1973), who found that under certain conditions, energy is readily transferred from the incident inertia–gravity wave to both a random field of scattered inertia–gravity waves and Kelvin waves trapped to the vertical coast. These studies demonstrate that scattering occurs when the incident wave, scattered wave, and bathymetry have wavenumbers such that a resonance condition is satisfied:

$$k_{\text{incident}} + k_{\text{topo}} = k_{\text{scattered}}, \tag{1}$$

where the sign of $k_{\text{scattered}}$ is restricted by the nature of the CTW to propagate with shallow water to the right (left) in the Northern (Southern) Hemisphere. As the topography is stationary in time, wave scattering from topography requires that the frequencies of the incident and scattered waves are identical.

Here, we extend the results of Howe and Mysak (1973) to the stratified ocean using idealized numerical simulations of mode-one inertia–gravity waves incident on a corrugated coast. We also explore the scattering of the Kelvin wave into a mode-one CTW at superinertial frequencies. We find that in both cases, the generation of CTW can be well predicted according to Eq. (1), and that even though the energy scattered into CTW may be relatively small, their current amplitudes are comparable to those of the generating waves, meaning that they are likely to be locally important.

Section 2 details the linear physics of flat-bottom and coastally trapped waves, section 3 describes the simulation setups and energetic analyses that are performed, and sections 4 and 5 present the results from simulations of flat-bottom mode-one waves and Kelvin waves incident at a corrugated coast. We discuss the implications of these results on realistic bathymetry in section 6 and discuss broader context and implications in section 7.

2. Linear physics

a. Internal tides in a flat-bottom ocean

In a horizontally uniform ocean, spatially separable solutions to the linearized, inviscid Navier–Stokes equations can be found by solving

$$\frac{d^2\hat{w}}{dz^2} + |\boldsymbol{\kappa}|^2 \frac{N^2 - \sigma^2}{\sigma^2 - f^2}\hat{w} = 0, \tag{2}$$

where $w = \hat{w}(z)e^{i(\boldsymbol{\kappa}\cdot\mathbf{x} - \sigma t)}$ is the vertical velocity (Gill 1982), $\boldsymbol{\kappa} = (k, l)$ is the horizontal wavenumber vector, and σ is the wave frequency. For a flat-bottom ocean with a rigid lid, the boundary conditions are

$$\hat{w}(0) = \hat{w}(-h) = 0. \tag{3}$$

Solutions to this Sturm–Liouville problem are inertia–gravity waves in the form of flat-bottom vertical modes. The vertical modes are one dimensional, with higher modes characterized by having more zero crossings. Without the loss of generality, the wave can be aligned with the x axis, and the structure of the horizontal currents $\hat{u}$ can be derived from $\hat{w}$ by employing the continuity equation:

$$\hat{u} = \frac{i}{k}\frac{d\hat{w}}{dz}. \tag{4}$$

Flat-bottom modes are frequently used to represent internal tides in the open ocean, where bathymetric variations are small on the horizontal scales of low-mode internal tides. For $f = 1 \times 10^{-4}$ rad s^{-1} and an idealized stratification profile $N(z)$, with a peak at the pycnocline (Fig. 1b), the first three flat-bottom modes [found by discretizing and solving Eq. (2) as an eigenvalue problem] are shown in Fig. 1c. The wavelength of the mode-one wave with a frequency of 1.36×10^{-4} rad s^{-1} is 335 km.

b. Internal tides at the coast

At the coast, cross-shelf bathymetric variations are significant enough that the cross-shelf and vertical dimensions cannot be separated. Assuming alongshelf (x) wave propagation, the linearized governing equations for the two-dimensional structure in the y–z plane across the coastal margin can be written as follows:

$$\frac{\partial^2\hat{p}}{\partial y^2} + (f^2 - \sigma^2)\frac{\partial}{\partial z}\frac{1}{N^2}\frac{\partial\hat{p}}{\partial z} - k^2\hat{p} = 0, \tag{5}$$

where $p(\mathbf{x}, t) = \hat{p}(y, z)e^{i(kx - \sigma t)}$ is the pressure mode and k is the alongshore wavenumber. This equation is solved subject to the no normal flow boundary condition at the bottom:

$$\frac{1}{N^2}\frac{\partial\hat{p}}{\partial z} = -\frac{H_y}{f^2 - \sigma^2}\left(\frac{\partial\hat{p}}{\partial y} + \frac{kf}{\sigma}\hat{p}\right) \quad \text{at} \quad z = -H(x), \tag{6}$$

a linearized free surface:

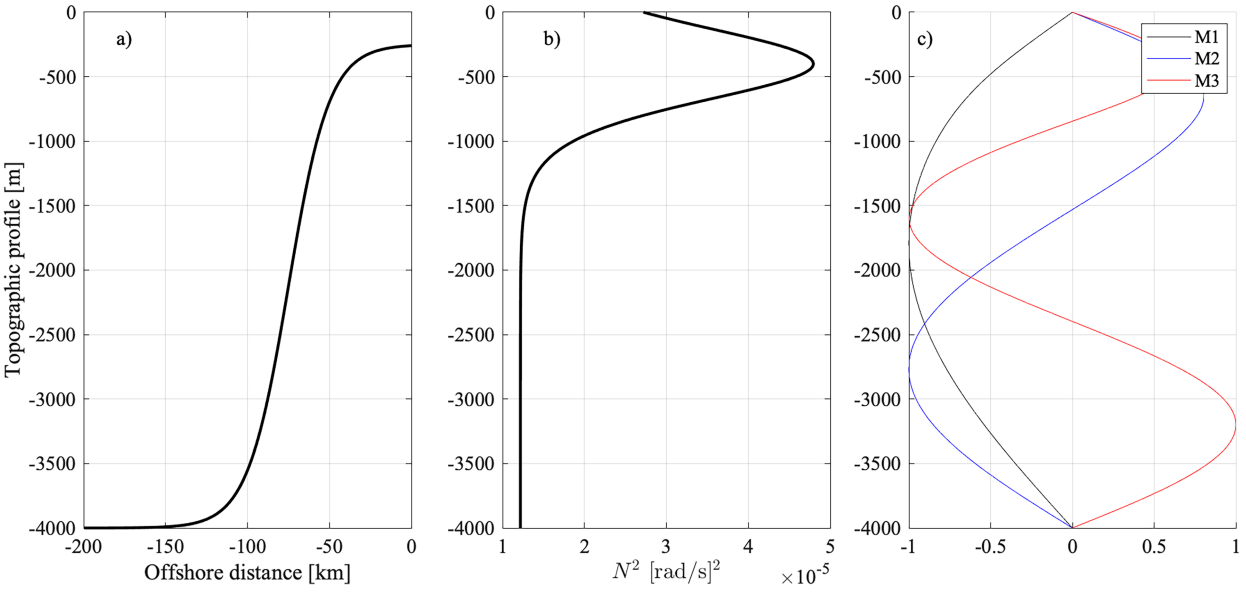

FIG. 1. (a) Topographic profile and (b) stratification used in models; (c) vertical velocity structure of first three flat-bottom modes associated with this stratification.

$$\tilde{w} = i\sigma\frac{\hat{p}}{g\rho_0} \quad \text{at} \quad z = 0, \tag{7}$$

no flow through the coastal boundary:

$$\frac{\partial\hat{p}}{\partial y} = -\frac{fk}{\sigma}\hat{p} \quad \text{at} \quad x = 0, \tag{8}$$

and, for subinertial frequencies, a decaying signal far offshore:

$$\hat{p} \to 0 \quad \text{at} \quad y \to \infty. \tag{9}$$

Solutions are two-dimensional coastally trapped waves, with higher modes having more zero crossings in the offshore direction.

Under certain conditions, when the parameter $H_y N_{\text{bot}}/f \gtrsim 1$, coastally trapped waves can exist at superinertial frequencies (Huthnance 1978; Chapman 1983). In this case, solutions are subject to an offshore boundary condition of a superposition of radiating flat-bottom modes, such that

$$p(x, z) = \sum_n a_n \hat{p}_n(z)\exp(ik_n x) \tag{10}$$

(Dale and Sherwin 1996). This enables coastally trapped waves to "leak" energy into radiating inertia–gravity waves, thus losing energy as they propagate along a coastal boundary. Mathematically, this appears as a complex alongshore wavenumber k_n, causing the amplitude of the coastally trapped component to decay with distance alongshore. In this sense, the coastal "modes" are coupled to the inertia–gravity wave continuum.

Equation 5 is solved numerically following the u–p method described in Dale et al. (2001), which avoids spurious singularities near $\sigma = f$. A forcing with specified frequency and alongshelf wavelength is added to the homogeneous equation, and the amplitude of the model response is calculated. In this manner, a resonance scan is undertaken, spanning frequencies and wavenumbers. We have solved these equations using the stratification and topographic profile shown in Fig. 1. Both flat-bottom inertia–gravity wave (IGW) modes and CTW modes appear as lines of elevated resonance, tracing the wave dispersion curves (see Fig. 2). Mode-one and higher CTW dispersion curves start at zero frequency and wavenumber, crossing the inertial period with wavelengths of 330 km ($k > 1.9 \times 10^{-5}$ rad m^{-1}) and smaller. Freely propagating flat-bottom IGW modes are also present in the resonance scan and are traced by red dashed curves in the figure. Refractively trapped edge waves bifurcate from the mode-one vertical mode at periods shorter than around 6 h, with the relatively high frequencies arising due to the short shelf width used in this study (Ke and Yankovsky 2010).

The presence of the coastal boundary supports the propagation of waves at both sub- and superinertial frequencies. At subinertial frequencies, only CTW can propagate; however, at superinertial frequencies, both freely propagating IGW and CTW can exist. Superinertial CTWs are coupled to the flat-bottom IGW vertical modes, which form the offshore boundary condition and enable the radiation of energy into the open ocean. Some limitations on the spectrum and propagation angles of the vertical modes to which the CTW can couple can be determined from Fig. 2, as the horizontal wavelengths of the vertical modes must be smaller than those of the CTW, and their propagation angles are determined by matching the alongshore component of the wave to the CTW wavelength. For example, for the stratification and bathymetry used to create Fig. 2, the mode-one CTW along a uniform shelf can couple only with mode two and higher flat-bottom IGW modes, which would have to propagate at oblique angles

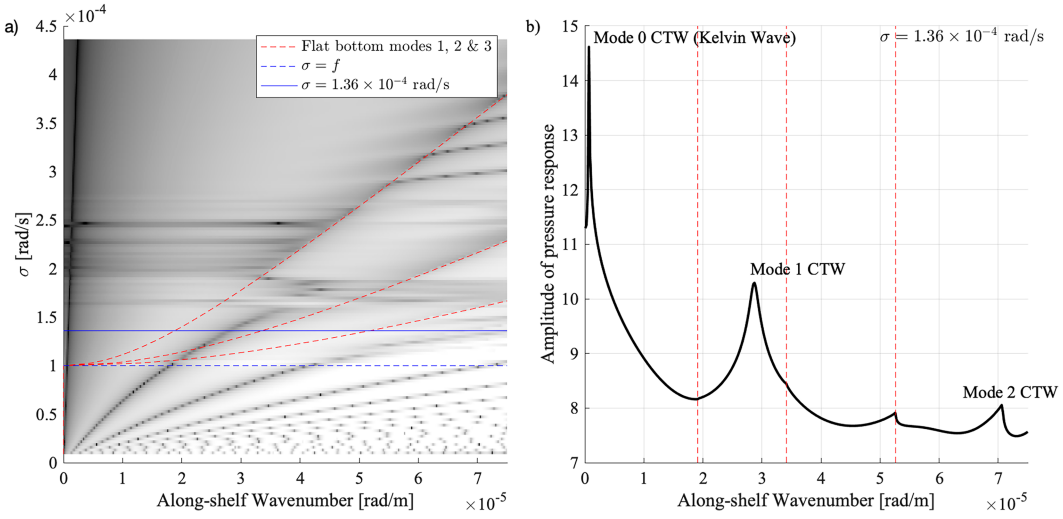

FIG. 2. Resonance scan from linear theory, following Dale et al. (2001). (a) Free modes are identified by peaks in model variance, appearing as darker lines in σ–k space. Red dashed lines indicate the predicted dispersion curves for the deep ocean offshore flat-bottom modes 1–3 for this stratification. The blue dashed line is the inertial frequency. (b) The pressure response of the model at a range of wavenumbers for $\sigma = 1.36 \times 10^{-4}$ rad s^{-1} [indicated by solid blue line in (a)] is given in the right panel, showing peaks for CTW modes 0, 1, and 2 and flat-bottom modes 2 and 3. Vertical red dashed lines indicate predicted flat-bottom mode 1–3 wavenumbers.

with respect to the bathymetry such that their alongshelf scales match that of the CTW.

In what follows, we pick a nominal frequency of $\sigma = 1.36f$, where $f = 1 \times 10^{-4}$ rad s^{-1}. The chosen wave frequency is superinertial and subcritical with respect to the topographic profile. For $\sigma/f = 1.36$, the alongshelf wavenumber of the mode-one CTW is 2.75×10^{-5} rad m^{-1}, or about 228 km, and of mode two is 7.5×10^{-5} rad m^{-1}, or about 83 km. The group velocity of the mode-one CTW at $\sigma/f = 1.36$ is calculated from the slope of the resonant line to be $c_g = \Delta\sigma/\Delta l = 2.28 \times 10^{-5}/0.64 \times 10^{-5} = 3.56$ m s^{-1}.

3. Model setup and analyses

We perform a series of numerical simulations that are designed to explore the scattering of wave energy at corrugated coastal topography. Simulations are run using a primitive equation numerical model, the MITgcm (Marshall et al. 1997), with stratification and cross-shelf bathymetric profile as shown in Fig. 1.

Two types of simulation are performed. In the first, we examine the interaction of a flat-bottom mode-one IGW incident on a corrugated coast at a range of angles of incidence, representing the interaction of the low-mode internal tide with the coast. In the second set of simulations, we examine the scattering of the topographically modified Kelvin wave (the gravest alongshelf propagating CTW mode) into CTW mode one at the same corrugations, representing the interaction of the barotropic tide with corrugated coastal bathymetry. In both sets of experiments, the wavelengths of the topographic corrugations are systematically varied between simulations.

a. *Simulation setup for incident internal tides on a corrugated coast*

These simulations are designed to model the interaction of a low-mode internal tide with the coastal boundary at a range of incident angles, as varying the angle of incidence causes the alongshelf projection of the incident wavelength to change. In each simulation, the alongshelf corrugations in the coastal boundary are sinusoidal, with topographic wavelengths ranging from 20 to 700 km.

The simulations are configured for a coast in the Northern Hemisphere, where the y direction is offshore, and coastally trapped waves are expected to propagate in the positive x direction (Fig. 3). The vertical structure and wavenumber of the mode-one IGW in the stratification profile (Fig. 1) are calculated by numerical solution to Eq. (2) at a frequency of $\sigma = 1.36 \times 10^{-4}$ rad s^{-1}. Two mode-one IGW wavelengths (around 670 km) offshore of the coast, we define a 1200-km-long forcing line where forcing terms are added to the u- and v-momentum equations to generate currents consistent with the modal structure. The alongshelf wavenumber on the forcing line is determined from the relation

$$k^{\theta}_{\mathrm{IGW}} = |\boldsymbol{\kappa}|\sin\theta, \tag{11}$$

where θ is the angle of propagation of the generated wave with respect to a line perpendicular to the coast and $|\boldsymbol{\kappa}|$ is the wavenumber magnitude of the mode-one IGW. Simulations are performed with $\theta = [-60°, -40°, -20°, 0°, 20°, 40°, 60°]$, where positive θ corresponds to the alongshelf component of the incident wave in the direction of CTW propagation (forward simulation) and negative θ corresponds to the alongshelf component of the incident wave in the opposite direction of

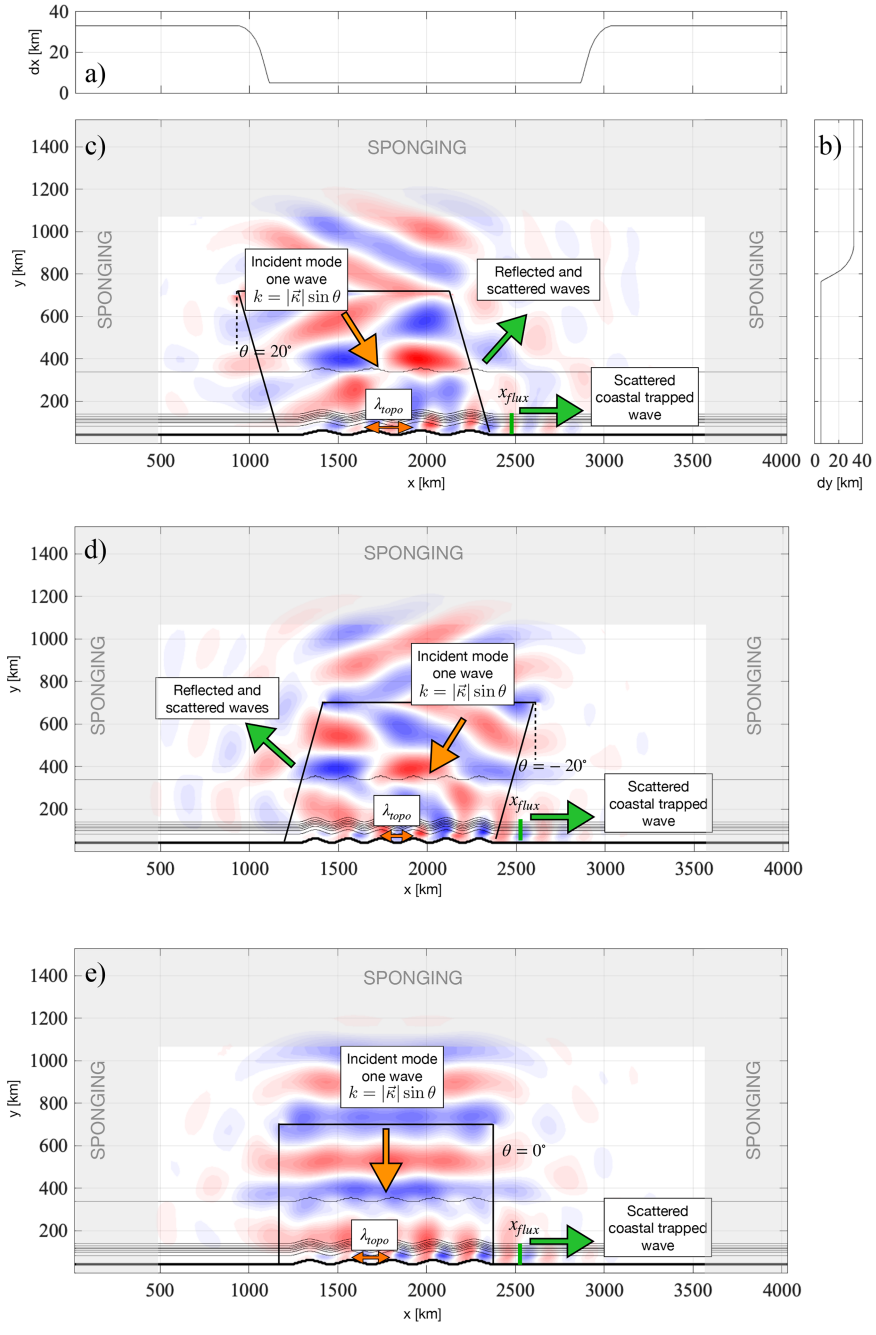

FIG. 3. Horizontal grid resolution in the (a) alongshelf and (b) cross-shelf directions for simulations. Snapshots of alongshelf surface currents at resonance for (c) $\theta = 20°$ and $\lambda_{\text{topo}} = 277$ km; (d) $\theta = -20°$ and $\lambda_{\text{topo}} = 184$ km; and (e) $\theta = 0°$ and $\lambda_{\text{topo}} = 231$ km. Shaded regions indicate where numerical sponging is applied.

CTW propagation (backward simulations). The velocities along the forcing line are prescribed as follows:

$$u = u_0 \hat{u}(z) \cos(k^{\theta}_{\text{IGW}} x - \sigma t),$$

$$v = u_0 \hat{u}(z) \frac{f}{\sigma} \sin(k^{\theta}_{\text{IGW}} x - \sigma t).$$

The incident mode-one currents have magnitudes of around 0.003 m s^{-1}, so nonlinear effects in the model are negligible. The currents that are forced along this line generate waves that radiate in both directions: toward and away from the coast. The waves that propagate offshore are damped by a sponge layer at the domain boundaries, while the waves that

propagate toward the coast have angles of incidence equal to θ; three examples of the simulation setup are shown in Fig. 3 for $\theta = -20°$, 0°, and 20°. The zonal location of corrugations along the coast is moved for different values of θ so that the corrugations remain located within the main beam of the incident internal waves.

The group velocity of the incident mode-one IGW is used to calculate the time required for the generated wave to reach the shelf. Simulations are run for five wave periods after the wave impacts the shelf (ranging from 183 h for $\theta = \pm 60$ to 123 h for $\theta = 0$).

Lateral corrugations in the shelf break are generated by displacing the cross-shelf profile from the coast by a sinusoid with amplitudes of 20 km for the main runs (spanning all θ). A further pair of simulations with promontory amplitudes of 10 and 40 km were undertaken for $\theta = 20°$ to test the impact of promontory amplitude on scattering. This mechanism for generating the coastal corrugations forms a series of promontories, whose "sides" are steeper than the rest of the slope. For each angle of incidence, 30 simulations are run with the wavelengths of the corrugations λ_{topo} spanning 20–700 km in increments of 23 km (we note that the 20-km simulation is only marginally resolved at the horizontal grid resolution of our simulations). Integer multiples of corrugation wavelengths are used to avoid the formation of discontinuities in the bathymetry at the edge of the corrugations. As the beam has a width of around 1200 km, the number of topographic corrugations that can fit within the beam depends on the topographic length scale: short length scales have around 60 promontories within the beam, while the longest length scales only have one. In total, 240 simulations were performed spanning all values of θ, λ_{topo}, and promontory amplitude.

To identify and separate the incident, reflected, and scattered wave components, several complementary simulations were also run. In the *no-shelf* (NS) simulations, the coast is removed entirely, and the domain is extended to the south with a numerical sponge such that all incident energy is absorbed. The *no-corrugation* simulations retain the coast and shelf bathymetry but remove the coastal corrugations. Both sets of simulations are run for all angles of incident wave energy.

To prevent the influence of reflected wave energy from the open boundaries of the domain, the grids are telescoped near the edges and numerical sponges are applied. Derived quantities such as wave flux are calculated in the interior of the domain away from regions of telescoping and sponging. The interior horizontal resolution is 5 km, and the vertical resolution varies from 25 m near the surface to 300 m at depth. Simulations are run in hydrostatic mode with free-slip boundaries at the topography. Model diffusivities and viscosities are set to maintain numerical stability, taking values of 1×10^3 m^2 s^{-1} in the horizontal, and 1×10^{-1} m^2 s^{-1} for viscosity in the vertical, and 1×10^{-6} m^2 s^{-1} for diffusivity in the vertical.

b. Simulation setup for incident Kelvin wave on a corrugated coast

A further 30 simulations were performed to quantify the interaction of the topographically modified Kelvin wave with corrugations of varying length scales. The bathymetry was created in the same manner as for the incident internal tide simulations, but in this case, a Kelvin wave is forced in a region upwave (i.e., to the west of the corrugations in this Northern Hemisphere simulation) of the corrugations and allowed to propagate into the corrugated region (Fig. 4). Depth uniform alongshore currents in the forcing region are specified to have the structure of a Kelvin wave along a straight vertical coast of depth H:

$$u = u_0 e^{-y/L_D}, \tag{12}$$

where $L_D = \sqrt{gH}/f$ is the deformation radius. The forcing region is one Kelvin wavelength long ($2\pi c_p/\omega = 9150$ km) and is located one wavelength west of the corrugations. The Kelvin wave structure is a very close approximation to that of the gravest (mode-zero) CTW along this sloping bathymetry, and the currents adjust to a dynamically consistent freely propagating structure as the wave propagates out of the forcing region before impacting the corrugations. Alongshore currents have magnitudes of around 0.025 m s^{-1}, thus maintaining linear dynamics. The simulations are run for 3.2 days, during which time the Kelvin waves develop in the forcing region and propagate across the corrugated region to the downwave boundary where they are dissipated in numerical sponges.

c. Analysis and resonance scans

The wave energy flux is defined as

$$\mathscr{F} = \frac{1}{T_p}\int_{T-T_p}^{T}\int_{-h}^{0} \mathbf{u}p \, dz dt, \tag{13}$$

where T_p is the wave period. We anticipate that incident mode-one IGW wave energy will both reflect and scatter into different wave modes, including higher IGW modes and CTW. On a uniform coast, wave scattering to high modes occurs when the coast deviates from a straight vertical wall (Kelly et al. 2013). To make estimates of the fraction of incident internal tide energy scattered into CTW by the corrugations, we linearly decompose the currents and pressures into the incident wave, straight-coast, and corrugated-coast components, denoted by subscripts i, rs, and rc, respectively:

$$\mathbf{u} = \mathbf{u}_i + \mathbf{u}_{\text{rs}} + \mathbf{u}_{\text{rc}}, \tag{14}$$

$$p = p_i + p_{\text{rs}} + p_{\text{rc}}. \tag{15}$$

Subsets of the decomposed fields are derived by differences from the NS and no-corrugation (NC) simulations. The currents and pressures associated with the NS simulations ($\mathbf{u}_{\text{NS}}$, p_{NS}) are associated with the incident wave:

$$\mathbf{u}_{\text{NS}} = \mathbf{u}_i, \tag{16}$$

$$p_{\text{NS}} = p_i. \tag{17}$$

The currents and pressures associated with the reflected and scattered wave field from a straight coast (subscript rs) can be computed using the NC and NS simulations such that

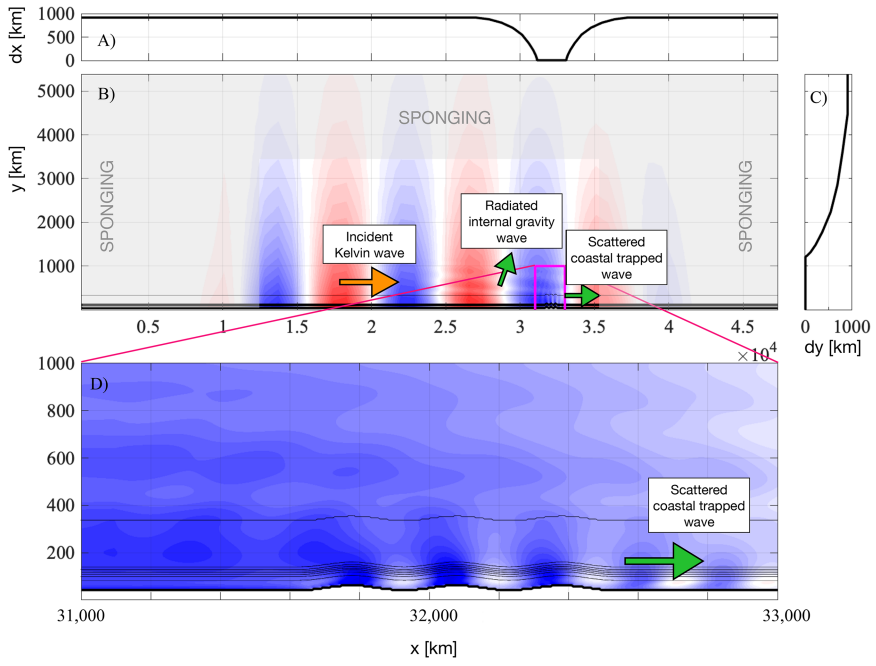

FIG. 4. MITgcm model setup for Kelvin wave incident on corrugated shelf. Horizontal grid resolution in the (a) alongshelf and (b) cross-shelf directions for simulations. Red and blue colors are alongshelf currents after 3 days for simulation with $\lambda_{\text{topo}} = 300$ km, with a color axis range of ± 0.025 m s^{-1}. Shaded regions indicate where numerical sponging is applied.

$$\mathbf{u}_{\text{rs}} = \mathbf{u}_{\text{NC}} - \mathbf{u}_i, \tag{18}$$

$$p_{\text{rs}} = p_{\text{NC}} - p_i. \tag{19}$$

The rs field includes both scattered (i.e., to high vertical modes) and specularly reflected components. The decomposition between the full and incident fields is not defined over the shelf and slope region, where the bathymetry has different depths between the NS, NC, and full simulations; as such, we take care to ensure that the rs field is only considered away from the coastal bathymetry where the depths in all simulations are identical.

The currents and pressures associated only with the effects of the corrugations are found as the difference between the full and no-corrugation simulations:

$$\mathbf{u}_{\text{rc}} = \mathbf{u} - \mathbf{u}_{\text{NC}}, \tag{20}$$

$$p_{\text{rc}} = p - p_{\text{NC}}. \tag{21}$$

We refer to these as scattered waves, as most specular reflection occurring in the simulations is accounted for along the straight coast. However, we note that the specularly reflected component is expected to be smaller in the full simulation compared to the no-corrugation simulation both due to increased viscous dissipation at the corrugated coast (with greater impact at smaller length scales) and due to the effects of resonance, where some of the incident wave energy is scattered rather than reflected. As a result, the scattered wave field calculated using this approach underestimates the flux in regions when viscous dissipation along the corrugations is large and where specular reflection is nonzero, i.e., offshore of the coast. Alternative approaches to calculating the CTW flux would be to fit the fields downstream of the corrugations to the predicted CTW from section 2 (e.g., Kelly and Ogbuka 2022), or to isolate the topographic (nondivergent) CTW modes by decomposing the flow into rotating and divergent components, as proposed by Tanaka (2023). Though these methods may have some advantages over the present approach, in the idealized scenario considered here, our approach of considering differences between the various simulations is sufficient.

With the decomposition defined in Eq. (15), the flux becomes

$$\begin{aligned}\langle \overline{\mathbf{u}p} \rangle = {} & \langle \overline{\mathbf{u}_i p_i} \rangle + \langle \overline{\mathbf{u}_i p_{\text{rs}}} \rangle + \langle \overline{\mathbf{u}_i p_{\text{rc}}} \rangle \\ & + \langle \overline{\mathbf{u}_{\text{rs}} p_{\text{rs}}} \rangle + \langle \overline{\mathbf{u}_{\text{rs}} p_i} \rangle + \langle \overline{\mathbf{u}_{\text{rs}} p_{\text{rc}}} \rangle \\ & + \langle \overline{\mathbf{u}_{\text{rc}} p_{\text{rc}}} \rangle + \langle \overline{\mathbf{u}_{\text{rc}} p_{\text{rs}}} \rangle + \langle \overline{\mathbf{u}_{\text{rc}} p_i} \rangle .\end{aligned} \tag{22}$$

Angle brackets indicate depth integrals, while overlines are time averages over the final period of the simulation. It will be shown that the cross terms are nonnegligible for these simulations, as the wave fields are not well represented by plane waves.

The energy flux components are calculated for each simulation. An estimate of the integrated scattered coastally trapped wave flux is determined by evaluating

$$\mathscr{F}_{\text{CTW}} = \int_0^{250\text{km}} \langle u_{\text{rc}} p_{\text{rc}} \rangle|_{x=x_{\text{flux}}} \, dy, \tag{23}$$

where x_{flux} is located 70-km downwave (i.e., to the east) of where the corrugations stop, a location far enough away from the evanescent currents around the corrugations (Fig. 3). The incident mode-one inertia–gravity wave flux is defined as

$$\mathscr{F}_{\text{IGWi}} = -\int_0^{L_x} \langle v_i p_i \rangle|_{y=250\text{km}} dx, \tag{24}$$

where L_x is the length of the computational domain (integration lines are indicated in magenta in Fig. 5).

A similar decomposition is undertaken for the simulations of an incident Kelvin wave on the corrugations, but this time only one additional simulation, the no-corrugation simulation, is required. We then define the scattered wave field as Eq. (21), with $\mathbf{u}_i = \mathbf{u}_{\text{NC}}$ in this case. The total flux is

$$\langle \overline{up} \rangle = \langle \overline{u_i p_i} \rangle + \langle \overline{u_i p_{\text{rc}}} \rangle + \langle \overline{u_{\text{rc}} p_i} \rangle + \langle \overline{u_{\text{rc}} p_{\text{rc}}} \rangle, \tag{25}$$

and the CTW flux is calculated to the east of the corrugations using Eq. (23) as for the incident internal wave simulations. The incident flux is computed at $x = 31\,200$ km, about 120-km upwave of the corrugations:

$$\mathscr{F}_{\text{KWi}} = \int_0^{250\text{km}} \langle (u_i + u_{\text{rc}})(p_i + p_{\text{rc}}) \rangle|_{x=31200\text{km}} dy. \tag{26}$$

As for the decomposition for incident internal tides, the interpretation of $\langle \overline{u_{\text{rc}} p_{\text{rc}}} \rangle$ as the scattered flux is not strictly accurate, as the "background" Kelvin wave field that is being removed is overestimated in the no-corrugation simulations compared to the corrugated simulations, where some of the incident energy has both been dissipated at the corrugations and scattered into coastal trapped waves (at resonance). As such, $\langle \overline{u_{\text{rc}} p_{\text{rc}}} \rangle$ is anticipated to be an underestimate of the scattered flux.

4. The reflection and scattering of an incident mode-one inertia–gravity wave at a corrugated coast

The interaction of the incident IGW with the coastal bathymetry includes reflected and scattered components that superpose with the incident waves to generate a complex wave pattern and energy flux field (Figs. 3 and 5a). The incident flux is calculated directly from the no-shelf simulation (Fig. 5b) and shows inhomogeneities in the incident beam at scales of hundreds of kilometers. The flux calculated as the difference between the no-shelf and no-corrugation fields $\langle \overline{u_{\text{rs}} p_{\text{rs}}} \rangle$ shows specular reflection, with the outward beam having a smaller amplitude and radiating away from the coast at an angle (Fig. 5c). The cross terms, $\langle \overline{u_i p_{\text{rs}}} \rangle$ and $\langle \overline{u_{\text{rs}} p_i} \rangle$ (Figs. 5e,g), have components that tend to mostly cancel one another in the offshore direction and reinforce one another in the alongshore direction, creating an alternating pattern of alongshore flux that is banded in the offshore direction, as would be expected for a partially standing wave arising from the interaction of the incident and reflected waves.

The flux components associated with the rc field specifically relate to the impacts of topographic corrugations on the wave field and mostly represents the scattered field (though interpretations as such are inaccurate in regions where the specularly reflected component is nonzero (see section 3c). The wave flux $\langle \overline{u_{\text{rc}} p_{\text{rc}}} \rangle$ shows clear enhancement downwave of the corrugations for certain topographic length scales and angles of incidence, corresponding to the generation of superinertial coastally trapped waves (Fig. 5d). Away from the coast, the wave field is directed offshore with inhomogeneities in flux amplitude corresponding to corrugation scales. As for the reflected flux, the cross terms arising from the interaction of the scattered and incident wave field $\langle \overline{u_i p_{\text{rc}}} \rangle$ and $\langle \overline{u_{\text{rc}} p_i} \rangle$ (Figs. 5f,j) generate a standing wave pattern with bands of alternating alongshore flux in the offshore direction. The interaction between the reflected and scattered waves, which both propagate offshore but at different angles, is captured in the cross terms $\langle \overline{u_{\text{rc}} p_{\text{rs}}} \rangle$ and $\langle \overline{u_{\text{rs}} p_{\text{rc}}} \rangle$. Both terms are associated with onshore flux, reducing the total offshore flux associated with the reflected and scattered fields (Figs. 5h,i).

The influence of changing wave incidence angle and corrugation wavelengths on CTW generation

The alongshelf scattered flux associated with the corrugations $\mathscr{F}_{\text{CTW}}$ is enhanced for specific resonant topographic wavelengths, with peak fluxes occurring at wavelengths that become larger as the angle of incidence varies from −60° to +60° (Fig. 6). CTW fluxes are larger for backward incident internal waves compared to forward incident waves, where for promontories of 20-km amplitude, up to approximately 5% of the incident internal gravity wave energy is scattered into coastally trapped waves that transfer energy along the coast. Though these fluxes are small compared to the incident internal waves, the CTWs are a leading order process over the shelf and shelf-break, with currents on the shelf having similar magnitudes to the incident internal wave (Fig. 3).

Similar to Howe and Mysak (1973), the resonant topographic wavelength at which an obliquely incident internal wave generates mode-one coastally trapped waves is determined by the relationship as follows:

$$k_{\text{CTW}} = k_{\text{topo}} + k^{\theta}_{\text{IGW}}, \tag{27}$$

where k^{θ}_{IGW} is the alongshore wavenumber projected onto the coast at an angle of incidence θ [see Eq. (11)]. The angle of incidence of the internal wave determines its alongshelf wavelength such that $|k^{\theta}_{\text{IGW}}| \leq |k_{\text{IGW}}|$. For backward incident waves, $k^{\theta}_{\text{IGW}} < 0$, while for a normally incident wave, $k^{\theta}_{\text{IGW}} = 0$. In the latter case, CTWs are predicted to be generated when the topographic length scales match those of the generated wave. For a given bathymetric profile, the wavelengths of the coastally trapped wave modes are determined as solutions to Eqs. (5)–(9), and in this configuration, the mode-one CTW has been determined through the linear analysis in section 2b to have a wavelength of 228 km. For each of the resonant simulations (identified as peaks in Fig. 6), the wavelength of the generated CTW was calculated as the distance between the first two peaks in surface currents downwave of the topographic corrugations along a line at $y = 60$ km. These compare favourably to the values predicted in section 2b (Fig. 7); as the angle of incidence of the internal gravity wave changes, the topographic length scales required to satisfy

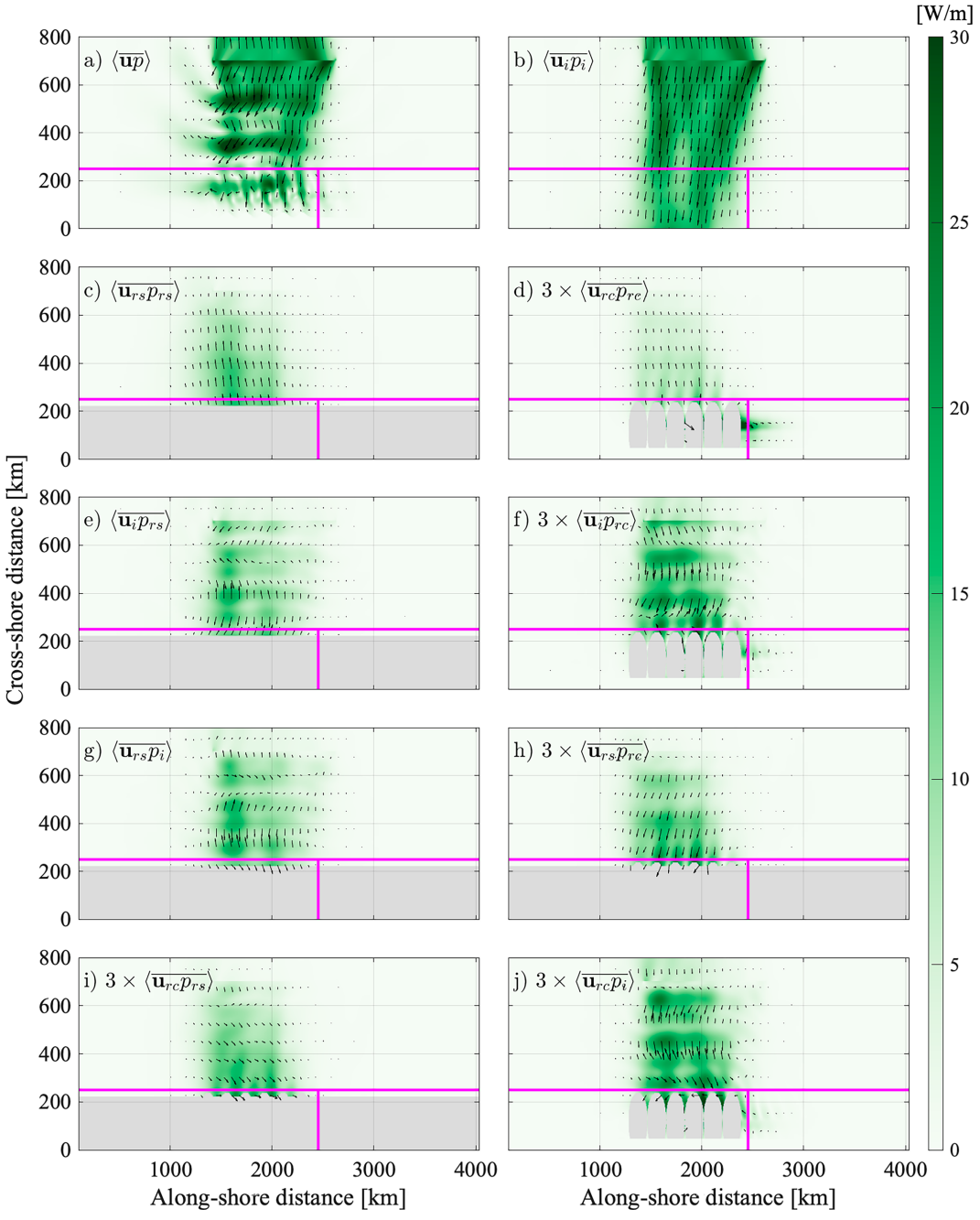

FIG. 5. Wave fluxes for $\theta = -20^\circ$ and $\lambda_{\text{topo}} = 184$ km, where a resonantly generated CTW occurs. Magenta lines indicate the boundaries along which fluxes are computed. Regions in gray indicate where the flux component is not well defined. (a) Total wave flux from full simulation; (b)–(j) each of the cross terms computed from fields derived from NS and NC simulations. Note that panels (d), (f), and (h)–(j) are scaled by 3 to make features clear on a common color scale.

Eq. (27) also change in a manner that is well described by this equation.

The energy fluxes presented in Fig. 6 were calculated over the final period of the simulation, which was set to be five periods after the incident IGW reached the coast. However, calculations of flux over each successive period since the wave reached the coast show that the flux was not at steady state by the fifth period. Using the predicted group velocity of the CTW from section 2b ($c_g = 3.56$ m s^{-1}), the distance over which CTW energy can propagate in five periods (around 64 h) is estimated to be 820 km, around 70% of the 1200-km width of the forcing region. As such, not all wave energy that

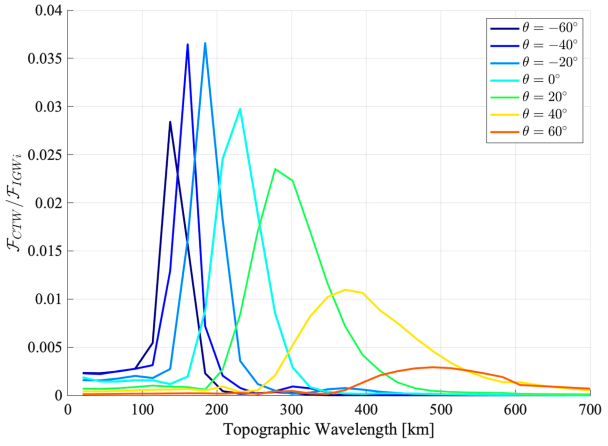

FIG. 6. Alongshelf CTW fluxes $\mathscr{F}_{\mathrm{CTW}}$ downstream of the corrugations at x_{flux}. Fluxes are normalized by the incident mode-one IGW flux $\mathscr{F}_{\mathrm{IGWi}}$.

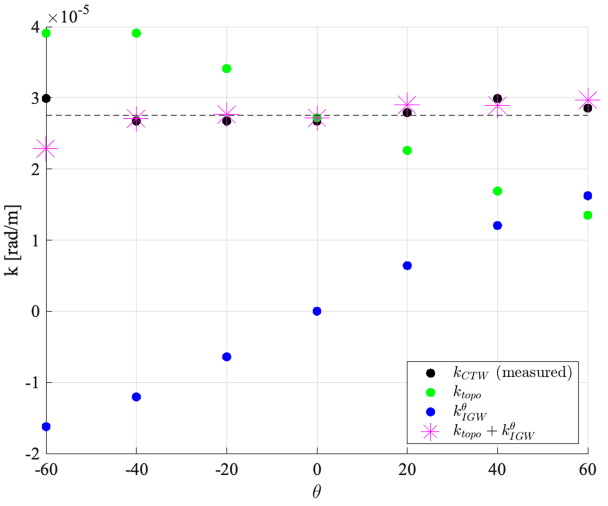

FIG. 7. Comparison of MITgcm model results to CTW scattering theory based on Howe and Mysak (1973). Blue dots show the alongshore wavenumber of the incident mode-one IGW ($k^{\theta}_{\mathrm{IGW}} = |\boldsymbol{\kappa}|\sin\theta$). Green dots show the topographic wavenumber k_{topo} for which the CTW response is maximum (see Fig. 6). Black dots are the measured wavenumber of the CTW downwave of the corrugations at resonance. The horizontal black dashed line shows k_{CTW} for the simulation forcing frequency ($\sigma = 1.36 \times 10^{-4}$ rad s^{-1}) based on linear theory (Fig. 2; $k_{\mathrm{CTW}} = 2.83 \times 10^{-5}$ rad m^{-1}). Magenta stars show the predicted k_{CTW} based on scattering theory ($k_{\mathrm{CTW}} = k_{\mathrm{topo}} + k^{\theta}_{\mathrm{IGW}}$).

was generated along the corrugations (specifically those generated at the western end of the corrugations) had enough time to reach x_{flux} by the time the simulation ended. To explore the sensitivity of our simulations on the number of coastline corrugations, a parallel simulation was run for $\theta = -20°$ at the resonant wavenumber, $k_{\mathrm{topo}} = 3.4 \times 10^{-5}$ rad s^{-1}, but with half of the number of corrugations compared to the standard run (i.e., three rather than six bumps). In this case, wave energy generated at the westernmost point of the corrugations is predicted to take less than four periods to propagate a distance of 600 km at the group speed to reach x_{flux}. Wave flux calculations from the simulation were steady after four periods, consistent with this prediction. Assuming the flux in the standard simulations after five periods is around 70% of what it would be at steady state, we find that the CTW flux normalized by the total incident IGW flux over the corrugated region is the same as when the number of corrugations is halved. This is expected for CTWs that are generated only along the corrugated region of the shelf and gives us confidence that the normalized fluxes presented in Fig. 6 are independent of the length of the corrugated region, or the number of bumps included.

In our simulations, CTW flux is nonzero for small topographic wavelengths even away from the resonant peak, especially so for backscattered simulations with large oblique angles. In these cases, the sharp transition from corrugations to noncorrugations along the shelf is spectrally broad, containing variance at all scales including the resonant scales. The generation mechanism here is analogous to the generation of shelf waves at a corner as noted in Klymak et al. (2016).

In addition to predicting the resonance condition, other predictions made for inertia–gravity waves in an unstratified ocean by Howe and Mysak (1973) may be verified in these stratified simulations. Howe and Mysak (1973) predict that the energy of scattered waves will increase linearly with promontory amplitude. Though we do not explore this extensively, by comparing the CTW flux at $\theta = 20°$ for promontory amplitudes of 10, 20, and 40 km, we find that the flux increases very close to linearly as predicted (Fig. 8). Furthermore, the relatively larger and narrower energy flux associated with backward scattering compared to forward scattering is also consistent with predictions inferred from considering the Howe and Mysak energy fluxes scattered from a coastal bathymetry having a Gaussian spectrum.

5. The scattering of the gravest CTW at coastal corrugations

The impact of astronomical forcing on the ocean induces tides that propagate as the gravest CTW, very closely approximating barotropic Kelvin wave solutions at a vertical wall. However, minor deviations from the Kelvin wave structure arise due to both the presence of nonvertical coastal boundaries and alongshelf coastal corrugations, and these contribute to internal tides both in the open ocean and at the coast.

Currents are nudged toward a Kelvin wave structure in the forcing region, which then propagates into the unforced region downwave along the coast, evolving into the gravest coastally trapped wave structure that is consistent with the cross-shelf bathymetric profile and stratification, having a wavelength of close to 9000 km as predicted by the resonance scans of section 2b (Fig. 2b). Offshore propagating internal tides are generated, radiating energy out of the leaky mode into the ocean interior (Fig. 4), consistent with predictions for internal tide generation at the coastal boundary (Baines 1982; Chapman 1983; Zemskova et al. 2024). The gravest CTW has current amplitudes of around

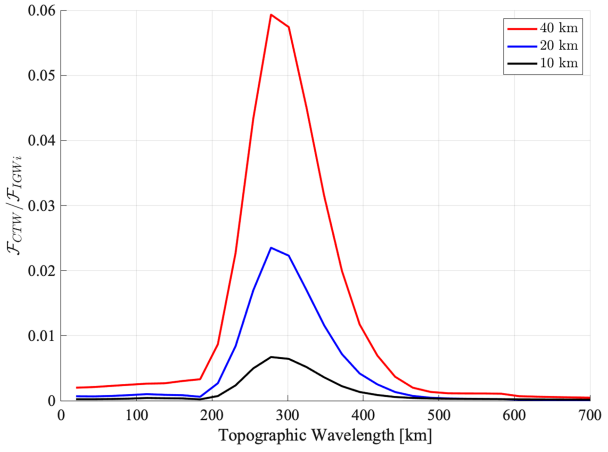

FIG. 8. As in Fig. 6, but for different amplitude promontories with $\theta = 20°$.

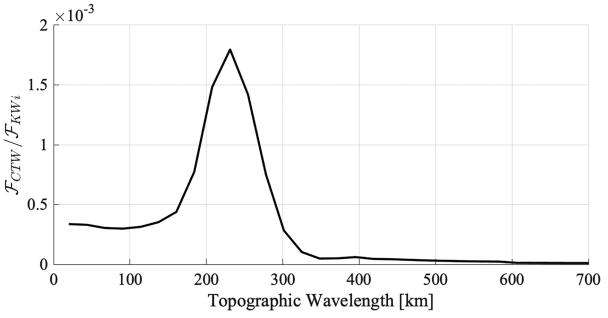

FIG. 9. Scattered alongshelf CTW flux integrated from $y = 0$–250 km at $x = x_{\text{flux}}$ and normalized by the upstream Kelvin wave flux (integrated out to the same distance) located to the west of the corrugations.

0.025 m s^{-1} and a corresponding alongshelf wave flux of 64 GW calculated just upstream of the corrugations.

Downstream of the corrugations, we compute the CTW fields by subtracting the wave currents and pressures associated with an uncorrugated shelf from those in the corrugated simulations. The CTW flux is computed as the time-averaged, depth-integrated product of the pressure and currents of the residual field [Eq. (23)], and resonance scans are created by integrating the alongshore flux at x_{flux}, located 70-km downwave of where the corrugations stop, out to 250-km offshore (Fig. 9). A clear peak appears at topographic scales of ≈230 km, matching the wavelength of the mode-one coastally trapped wave. The resonance condition equivalent to that for the incident inertia–gravity wave simulation [Eq. (27)] becomes

$$k_{\text{CTW}} \approx k_{\text{topo}}, \tag{28}$$

as $k_{\text{KW}} \ll k_{\text{topo}}$. This leads to resonance when the mode-one CTW and topographic scales match, as for the case of a normally incident flat-bottom mode (section 4a). The waves are apparent as perturbations to the large-scale currents associated with the gravest CTW close to and downwave of the corrugated bathymetry (Fig. 4).

As for the incident IGW cases, alongshore fluxes in these simulations are nonzero for small topographic wavelengths, even away from resonance (e.g., for corrugation scales less than 200 km). These fluxes are associated with the generation of a mode-one CTW at the transition from the corrugated to uncorrugated region, which is increasingly abrupt for shorter compared to larger topographic wavelengths. The spectral content of this transition is broad for short topographic wavelengths, including variance at a wide range of scales, resulting in the weak generation of CTW in our simulations.

6. Scales in realistic coastal bathymetry

The highly idealized bathymetry of the previous sections enables the identification of the underlying triad interactions on wave scattering at the coast; however, realistic bathymetries are much more complex, including a range of alongshelf length scales and cross-shelf slope profiles. As a first step toward assessing the relevance of this work to general oceanic conditions, we used the bathymetry of the West Coast of the United States and Canada to determine the length scales present in realistic bathymetry (Fig. 10). The bathymetry was derived by extracting the 500-m isobath from General Bathymetric Chart of the Oceans (GEBCO; GEBCO Compilation Group 2020) and then low-pass filtering the latitudes and longitudes of the coordinates over scales of around 340 km. The distances between the smoothed and original contour (Fig. 10b) were calculated as a function of distance along the contour, giving an estimate of the depth of the corrugations and their alongshelf length scales. Corrugations have amplitudes with typical values of 20–30 km and alongshelf wavelengths of around 100 km (though this value is dependent on the filter length). The power spectrum of the isobath corrugations has a slope a little steeper than −2, with no significant peaks. The range of scales present in the shelf bathymetry makes it likely that internal tides incident at almost any angle could excite CTW at some point along the coast. Close to the Mendocino Ridge (near 40°N), the most likely incidence angle is near oblique, as generation here leads to internal tides propagating north and south from this feature (Althaus et al. 2003). However, further to the north and south of the ridge, it is difficult to make any general predictions about the angles of incidence of the internal tide, especially in the presence of mesoscale variability, which will tend to refract the waves. This will alter both the amplitude and angle of incidence of the internal tide at any particular location along the coast in time, leading to intermittency in the generation of resonant CTW by this mechanism.

To the north of the ridge, forward scattering is anticipated as incident internal tides propagate in the same direction as coastally trapped waves, and as such topographic scales that are larger than those of the CTW would be expected to be generators, with rather less efficiency than if the waves were propagating with a southward component along the coast (Howe and Mysak 1973). To the south of the ridge, however, incident internal tides propagate in the opposite direction of CTW (backward scattering), and as such CTW would be expected to be relatively larger, occurring at topographic scales smaller than the CTW wavelength.

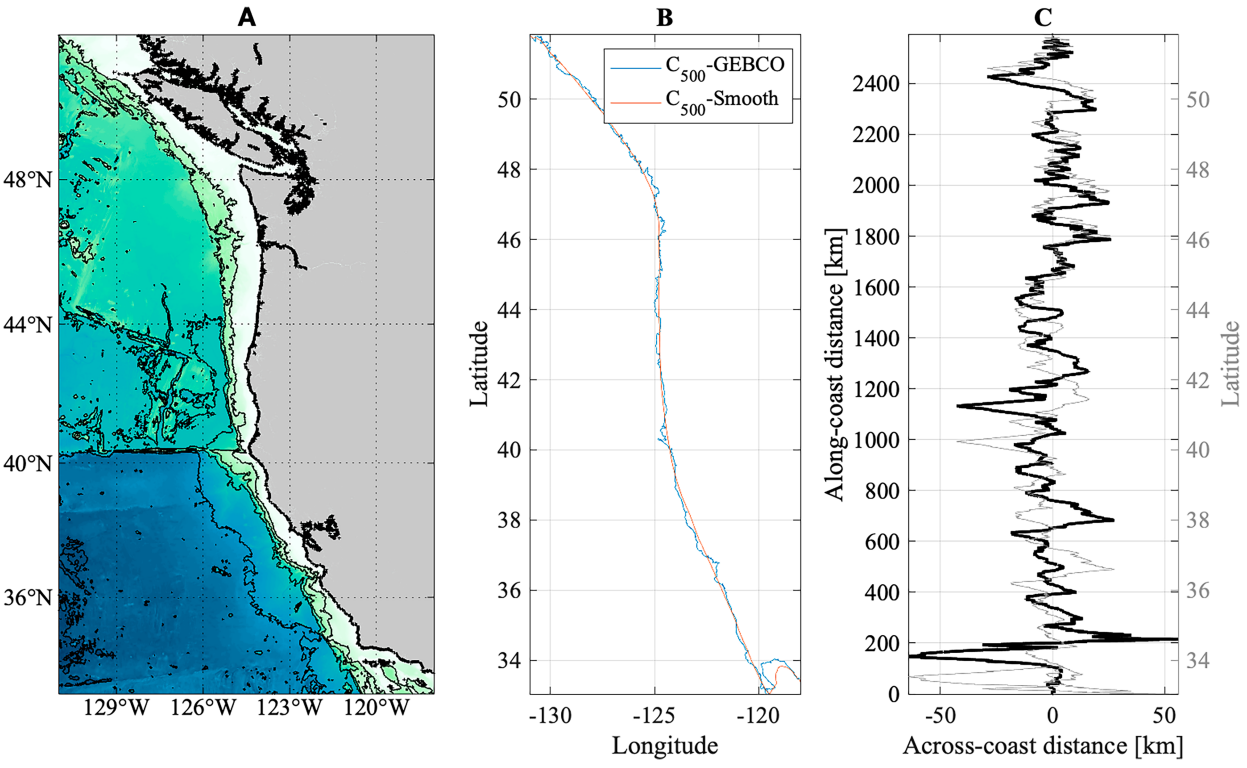

FIG. 10. (a) Bathymetry of the West Coast of the United States and Canada from GEBCO, (b) 500-m isobath in full resolution (blue) and ≈340-km smoothed (red), and (c) cross-shelf perturbations of 500-m isobath.

7. Discussion

In this paper, we have used idealized numerical simulations to demonstrate the generation of a superinertial mode-one CTW through the scattering of tidal motions at corrugated bathymetry. The stratification and cross-shelf bathymetric profile is such that the CTW dispersion curve reaches and passes above the inertial frequency. For this case, we have demonstrated that superinertial coastally trapped waves can be generated by the following:

1) The scattering of energy from a Kelvin wave at coastal corrugations that have length scales close to those of the CTW.
2) The scattering of energy from an incident mode-one IGW, such as those associated with the majority of energy in the internal tide, when the alongshelf wavenumber of the incident wave $k_{\mathrm{IGW}}^{\theta}$, topographic wavenumber k_{topo}, and CTW wavenumber k_{CTW} satisfy a resonance condition: $k_{\mathrm{CTW}} = k_{\mathrm{topo}} + k_{\mathrm{IGW}}^{\theta}$.

In both cases, the generated CTWs have currents that are comparable to the incident wave, forming a leading order process in the shelf/slope region. Calculations of the energy flux in the CTW account for less than 5% of the incident flux on the coast, but we emphasize the tremendous differences in length scales of the generating waves compared to the CTW that give rise to this apparently small value. Finally, we note that a third resonant case is predicted to occur along a uniform coast when the incident internal tide occurs at an angle such that $k_{\mathrm{IGW}} = k_{\mathrm{CTW}}$. In general, for the same mode, $k_{\mathrm{IGW}} < k_{\mathrm{CTW}}$ such that this condition can only be met by a higher-mode IGW generating a lower mode CTW (e.g., a mode-two IGW generating a mode-one CTW). In this case, the matching of vertical scales may affect the efficiency of the scattering process.

Though we have not explicitly considered it here, we anticipate that where shelf widths are wider, the transition of the tidal Kelvin wave to a mode-zero edge wave will affect resonant dynamics. In this case, the bathymetric profile and stratification may no longer support superinertial CTWs, and even if it does, the wave flux is concentrated over the shelf rather than the slope as for Kelvin waves (Ke and Yankovsky 2010). For mode-zero edge waves, changes in alongshelf bathymetry have been shown to give rise to the generation of freely propagating internal tides that transfer tidal energy away from the shelf (Yankovsky and Zhang 2017). Whether mode-one CTWs could also be resonantly generated in this case speaks to the broader question of the extent to which the unstratified results of Howe and Mysak (1973) can be applied in the stratified ocean and warrants a separate investigation.

The mechanisms discussed here may play a role in the loss of energy from low-mode incident internal tides at the coast, as well as the generation of coastal internal tides. As has been found in other studies examining the scattering of low-mode internal tide energy at topography (e.g., Müller and Xu 1992; St. Laurent and Garrett 2002), the fluxes carried by these waves are small compared to the generating flux, accounting

for less than 5% of the incident wave energy at resonance. However, the current amplitudes associated with the waves are comparable to the generating currents, and locally they are a leading order process (Fig. 3). Unlike the inertia–gravity waves considered in other scattering studies, superinertial CTWs are largely constrained to dissipate their energy along the coast, though some energy can "leak" back into the ocean's interior. The energy that propagates along the coast is susceptible to both boundary layer turbulence or further scattering as the waves propagate along a continually varying coastline, with direct implications for coastal mixing.

Our results are consistent with predictions made by Howe and Mysak (1973), who derived analytic expressions for the scattering of an incident inertia–gravity wave at a corrugated coast in an unstratified ocean. That theory makes predictions that we have not extensively tested, such as the relative magnitude of the scattered field being dependent on the parameter $\beta = (\overline{\zeta^2})^{1/2} f/c_p$, where $\overline{\zeta^2}$ is the variance in the coastal corrugations (see Fig. 8) and c_p is the phase speed of the Kelvin wave (or, by analogy in the stratified case, the phase speed of the wave into which energy is being scattered). At different latitudes or for waves with different phase speeds (e.g., associated with deeper or shallower bathymetry), we anticipate that the scattering efficiency may be different. However, a key limitation of the application to the theory described by Howe and Mysak (1973) to the stratified ocean is the vertical structure inherent in the stratified waves that we have considered in this work. Inertia–gravity wave scattering generally requires that both the vertical and horizontal wavenumbers as well as wave frequency must satisfy triad conditions. Our simulations have demonstrated that resonance occurs when the horizontal wavenumbers satisfy the triad condition for low-mode stratified waves, but further work is required to understand the efficiency of this process across all parameter space, in particular where the vertical scales of the IGW and CTW may be very different.

The generation of superinertial CTWs was found in the simulations of Klymak et al. (2016), who modeled the interaction of an incident mode-one wave on the Tasman Shelf. In those simulations, a shelf wave was excited in simulations with either realistic or idealized bathymetry. In the latter case, the CTW was generated at a corner of the idealized topography, irrespective of the angle of incidence of the internal tide. Our results are consistent with these findings, as such a corner includes a range of length scales that are capable of resonating with a broad range of angles associated with the incident internal waves. Similarly to Klymak et al. (2016), we used complementary no-corrugation and no-shelf simulations to isolate the wave fields associated with the incident and reflected/scattered signals. However, as discussed by Klymak et al. (2016), the presence of nonnegligible cross terms lends some ambiguity to our definitions of incident and reflected wave energy, as the cross terms that arise from the interactions of the wave fields also carry energy. The complex flux patterns that arise often resemble partially standing waves, with large alongshore components that are not associated with a single dynamic entity.

The generation of CTWs by both Kelvin waves and incident internal tides provides some insight on when and where these phenomena may be generated along a realistic coastline. Generation by the alongshelf propagation of a low-mode CTW occurs predictably at topographic promontories having the similar length scales to that of the higher mode CTWs, and thus, based on the structure of stratified CTWs predicted by linear theory, one might anticipate that generation will occur at relatively wider promontories on narrower shelves, compared to broader shelves. However, the locations and magnitude of generation by an incident shoaling internal tide are likely to be much more variable, depending sensitively on the length scales present in the coast and the angle of incident of the internal tide. Observations show that internal tides at the coast are highly intermittent, with the intermittency arising from the shoaling of remotely generated internal tides that propagate long distances through a time-varying mesoscale field (Nash et al. 2012). This intermittency changes not only the amplitude of the incident internal wave along the coast but also the angle of incidence, with the implication that the generation efficiency of superinertial CTWs along realistic coasts is expected to be similarly intermittent. Nevertheless, our results suggest that the scattering of barotropic and internal tides to CTWs should be considered as an integral component of internal tide dynamics in coastal regions.

Acknowledgments. This work was supported by the following NSF Grants for D. W., V. E. Z., and J. A. L.: OCE-1756752 and OCE-2220439. R. C. M. acknowledges funding from NSF under Grant OCE-1756781 and support from the Canada Research Chairs Program. The authors are grateful to two anonymous reviewers whose comments have improved this work.

Data availability statement. All files required to set up and configure representative simulations using MITgcm are available at Dalhousie University Dataverse: https://doi.org/10.5683/SP3/8CFSC1.

REFERENCES

Althaus, A. M., E. Kunze, and T. B. Sanford, 2003: Internal tide radiation from Mendocino Escarpment. *J. Phys. Oceanogr.*, **33**, 1510–1527, https://doi.org/10.1175/1520-0485(2003)033<1510:ITRFME>2.0.CO;2.

Baines, P. G., 1982: On internal tide generation models. *Deep-Sea Res.*, **29A**, 307–338, https://doi.org/10.1016/0198-0149(82)90098-X.

Brink, K. H., 1980: Propagation of barotropic continental shelf waves over irregular bottom topography. *J. Phys. Oceanogr.*, **10**, 765–778, https://doi.org/10.1175/1520-0485(1980)010<0765:POBCSW>2.0.CO;2.

——, 1986: Scattering of long coastal-trapped waves due to bottom irregularities. *Dyn. Atmos. Oceans*, **10**, 149–164, https://doi.org/10.1016/0377-0265(86)90004-7.

Chao, S.-Y., L. J. Pietrafesa, and G. S. Janowitz, 1979: The scattering of continental shelf waves by an isolated topographic irregularity. *J. Phys. Oceanogr.*, **9**, 687–695, https://doi.org/10.1175/1520-0485(1979)009<0687:TSOCSW>2.0.CO;2.

Chapman, D. C., 1983: On the influence of stratification and continental shelf and slope topography on the dispersion of subinertial coastally trapped waves. *J. Phys. Oceanogr.*, **13**, 1641–1652, https://doi.org/10.1175/1520-0485(1983)013<1641:OTIOSA>2.0.CO;2.

Dale, A. C., and T. J. Sherwin, 1996: The extension of baroclinic coastal-trapped wave theory to superinertial frequencies. *J. Phys. Oceanogr.*, **26**, 2305–2315, https://doi.org/10.1175/1520-0485(1996)026<2305:TEOBCT>2.0.CO;2.

——, J. M. Huthnance, and T. J. Sherwin, 2001: Coastal-trapped waves and tides at near-inertial frequencies. *J. Phys. Oceanogr.*, **31**, 2958–2970, https://doi.org/10.1175/1520-0485(2001)031<2958:CTWATA>2.0.CO;2.

de Lavergne, C., S. Groeskamp, J. Zika, and H. L. Johnson, 2022: The role of mixing in the large-scale ocean circulation. *Ocean Mixing*, M. Meredith and A. Naveira Garabato, Eds., Elsevier, 35–63, https://doi.org/10.1016/B978-0-12-821512-8.00010-4.

GEBCO Compilation Group, 2020: GEBCO 2020 Grid. British Oceanographic Data Centre, https://doi.org/10.5285/a29c5465-b138-234d-e053-6c86abc040b9.

Gill, A. E., 1982: *Atmosphere–Ocean Dynamics*. Vol. 30. Academic Press, 662 pp.

Howe, M. S., and L. A. Mysak, 1973: Scattering of Poincaré waves by an irregular coastline. *J. Fluid Mech.*, **57**, 111–128, https://doi.org/10.1017/S0022112073001059.

Huthnance, J. M., 1978: On coastal trapped waves: Analysis and numerical calculation by inverse iteration. *J. Phys. Oceanogr.*, **8**, 74–92, https://doi.org/10.1175/1520-0485(1978)008<0074:OCTWAA>2.0.CO;2.

Ke, Z., and A. E. Yankovsky, 2010: The hybrid Kelvin–edge wave and its role in tidal dynamics. *J. Phys. Oceanogr.*, **40**, 2757–2767, https://doi.org/10.1175/2010JPO4430.1.

Kelly, S. M., and S. Ogbuka, 2022: Coastal trapped waves: Normal modes, evolution equations, and topographic generation. *J. Phys. Oceanogr.*, **52**, 1835–1848, https://doi.org/10.1175/JPO-D-21-0220.1.

——, N. L. Jones, J. D. Nash, and A. F. Waterhouse, 2013: The geography of semidiurnal mode-1 internal-tide energy loss. *Geophys. Res. Lett.*, **40**, 4689–4693, https://doi.org/10.1002/grl.50872.

Klymak, J. M., H. L. Simmons, D. Braznikov, S. Kelly, J. A. MacKinnon, M. H. Alford, R. Pinkel, and J. D. Nash, 2016: Reflection of linear internal tides from realistic topography: The Tasman continental slope. *J. Phys. Oceanogr.*, **46**, 3321–3337, https://doi.org/10.1175/JPO-D-16-0061.1.

MacKinnon, J. A., and K. B. Winters, 2005: Subtropical catastrophe: Significant loss of low-mode tidal energy at 28.9°. *Geophys. Res. Lett.*, **32**, L15605, https://doi.org/10.1029/2005GL023376.

Marshall, J., A. Adcroft, C. Hill, L. Perelman, and C. Heisey, 1997: A finite-volume, incompressible Navier Stokes model for studies of the ocean on parallel computers. *J. Geophys. Res.*, **102**, 5753–5766, https://doi.org/10.1029/96JC02775.

Müller, P., and N. Xu, 1992: Scattering of oceanic internal gravity waves off random bottom topography. *J. Phys. Oceanogr.*, **22**, 474–488, https://doi.org/10.1175/1520-0485(1992)022<0474:SOOIGW>2.0.CO;2.

Nash, J. D., S. M. Kelly, E. L. Shroyer, J. N. Moum, and T. F. Duda, 2012: The unpredictable nature of internal tides on continental shelves. *J. Phys. Oceanogr.*, **42**, 1981–2000, https://doi.org/10.1175/JPO-D-12-028.1.

Simmons, H. L., R. W. Hallberg, and B. K. Arbic, 2004: Internal wave generation in a global baroclinic tide model. *Deep-Sea Res. II*, **51**, 3043–3068, https://doi.org/10.1016/j.dsr2.2004.09.015.

St. Laurent, L., and C. Garrett, 2002: The role of internal tides in mixing the deep ocean. *J. Phys. Oceanogr.*, **32**, 2882–2899, https://doi.org/10.1175/1520-0485(2002)032<2882:TROITI>2.0.CO;2.

Tanaka, Y., 2023: Energy conversion rate from subinertial surface tides to internal tides. *J. Phys. Oceanogr.*, **53**, 1355–1374, https://doi.org/10.1175/JPO-D-22-0201.1.

Yankovsky, A. E., and T. Zhang, 2017: Scattering of a semidiurnal barotropic Kelvin wave into internal waves over wide continental shelves. *J. Phys. Oceanogr.*, **47**, 2545–2562, https://doi.org/10.1175/JPO-D-16-0284.1.

Zemskova, V. E., R. C. Musgrave, and J. A. Lerczak, 2024: Internal tides at the coast: Energy flux of baroclinic tides propagating into the deep ocean in the presence of supercritical shelf topography. *J. Phys. Oceanogr.*, **54**, 1367–1387, https://doi.org/10.1175/JPO-D-23-0164.1, in press.